Bifurcated Structure of the Electron Diffusion Region in Three-Dimensional Magnetic Reconnection

Yi-Hsin Liu,[1] W. Daughton,[1] H. Karimabadi,[2] H. Li,[1] and V. Roytershteyn[2]
[1]*Los Alamos National Laboratory, Los Alamos, New Mexico 87545, USA*
[2]*SciberQuest, Del Mar, California 92014, USA*

(Received 2 January 2013; published 25 June 2013)

Three-dimensional kinetic simulations of magnetic reconnection reveal that the electron diffusion region is composed of two or more current sheets in regimes with weak magnetic shear angles $\phi \lesssim 80^\circ$. This new morphology is explained by oblique tearing modes which produce flux ropes while simultaneously driving enhanced current at multiple resonance surfaces. This physics persists into the nonlinear regime leading to multiple electron layers embedded within a larger Alfvénic inflow and outflow. Surprisingly, the thickness of these layers and the reconnection rate both remain comparable to two-dimensional models. The parallel electric fields are supported predominantly by the electron pressure tensor and electron inertia, while turbulent dissipation remains small.

DOI: 10.1103/PhysRevLett.110.265004 PACS numbers: 94.30.cp, 52.35.Vd, 96.60.Iv

The energy release driven by magnetic reconnection is important for a wide range of applications in space, laboratory, and astrophysical plasmas [1]. In high-temperature plasmas, reconnection involves a coupling between the macroscopic sheared magnetic field and the kinetic scales where the frozen-flux condition is violated within a *diffusion region*. The present understanding is based on a two-dimensional (2D) picture [2] in which the ions decouple from the field on the ion inertial scale, while electrons decouple within a much smaller layer where the frozen-flux condition is broken by electron inertia and nongyrotropic terms in the pressure tensor [3–6]. These electron layers can become highly extended [7–10], indicating an inherent coupling to the larger dynamics.

Extending these results to large three-dimensional (3D) systems introduces a number of complications. First, the 3D structure of reconnection remains uncertain, since the dynamics may proceed at multiple competing orientations in both the linear and nonlinear regimes, leading to a spectrum of interacting flux ropes [11–13]. Second, various types of kinetic instabilities which are excluded in 2D may drive turbulence in 3D and produce anomalous resistivity or viscosity [3]. For example, lower-hybrid instabilities can produce anomalous resistivity in certain regimes within neutral sheets [14]. And in the strong guide field regime, recent 3D kinetic simulations [15] of force-free current sheets have reported a fast growing electron shear instability, resulting in strong turbulent viscosity and associated broadening of the layer. However, the persistence of these effects in large systems remains uncertain, due to the limited spatial volume and relatively short time durations considered.

In this Letter, we reexamine these guide-field regimes using fully kinetic 3D simulations with volumes ∼300 × larger and durations over ∼12 × longer than previously considered [15], which is sufficient to distinguish between transient effects and to allow coupling to 3D flux ropes dynamics. We consider parameter regimes $\beta_e \equiv 8\pi n T/B^2 \sim 0.01 \rightarrow 0.2$ where force-free current layers are applicable and magnetic shear angles from $\phi = 28^\circ \rightarrow 180^\circ$. As discussed in Ref. [15], these weaker shear angles are relevant to the solar corona [16,17], the solar wind [18,19], and planetary magnetospheres [20–22]. Our results reveal a number of striking differences with the previous small-scale studies [15]. First, using a combination of linear theory and simulations, we demonstrate that the dominant instability is collisionless tearing, with no evidence of turbulent broadening in the electron layers. The only clear exception is within very thin layers where electron-ion streaming instabilities are triggered [23,24]. While these regions can drive localized bursts of turbulence at early time, it appears these streaming instabilities are difficult to maintain in large simulations due to the strong electron parallel heating in low-β reconnection [25]. Second, the fastest growing tearing modes occur at oblique angles for regimes with weak magnetic shear $\phi \lesssim 80^\circ$. This has dramatic implications for the 3D structure, since these modes gives rise to oblique flux ropes while simultaneously driving enhanced current at multiple resonance layers.

This physics persists into the nonlinear regime and gives rise to reconnection layers that are intrinsically 3D, with multiple electron diffusion regions embedded within a single ion-scale layer with Alfvénic inflow and outflow. While secondary tearing is observed within the electron layers, there is no evidence of the previously reported electron shear instability [15] and the measured anomalous resistivity remains small. As a consequence, the characteristic layer thickness, pressure agyrotropy [26], and reconnection rate all remain comparable to 2D simulations. The parallel electric field is balanced through the combined influence of electron inertia and the electron pressure tensor, but with one important difference. While 2D symmetric reconnection layers require a nongyrotropic contribution to the pressure tensor near the x-line [4–6], this symmetry constraint is removed in 3D, allowing temperature anisotropy additional flexibility to break the frozen-flux condition.

We consider force-free current layers with $\mathbf{B} = B_0 \tanh(z/\lambda)\hat{\mathbf{x}} + B_0[b_g^2 + \mathrm{sech}^2(z/\lambda)]^{1/2}\hat{\mathbf{y}}$, corresponding to a field of magnitude $B_0(1 + b_g^2)^{1/2}$ which rotates by an angle $\phi \equiv \cos^{-1}[(b_g^2 - 1)/(b_g^2 + 1)]$ across a layer with half-thickness λ. Here b_g is the relative magnitude of the imposed guide field. The initial distributions are Maxwellian with spatially uniform density n_0 and temperature ($T_i = T_e$). The ion population is stationary while the electrons have a net drift $\mathbf{U}_e$ to produce a current density $\mathbf{J} = -en_0\mathbf{U}_e$ consistent with $\nabla \times \mathbf{B} = 4\pi\mathbf{J}/c$. We consider the tearing stability of this configuration for an arbitrary wave vector $\mathbf{k} = k_x\hat{\mathbf{x}} + k_y\hat{\mathbf{y}}$ corresponding to oblique angle $\theta \equiv \tan^{-1}(k_y/k_x)$ and resonance surface $z_s/\lambda = -\tanh^{-1}[(1 + b_g^2)^{1/2}\sin\theta]$ where $F \equiv \mathbf{k}\cdot\mathbf{B} = 0$. In the outer region, the magnetohydrodynamic model is used to obtain an eigenmode equation [27] of the form $\tilde{\psi}'' = (k^2 + F''/F)\tilde{\psi}$, where $\tilde{\psi}(z)$ is the perturbed flux function at the oblique plane and $k^2 \equiv k_x^2 + k_y^2$. By combining the approximate solutions for $k\lambda \ll 1$ and $k\lambda \gg 1$ in the same manner as Ref. [28], we obtain

$$\Delta' \equiv \lim_{\epsilon\to 0}\frac{1}{\tilde{\psi}}\left[\frac{d\tilde{\psi}}{dz}\right]_{z_s-\epsilon}^{z_s+\epsilon} \approx \frac{2}{k\lambda^2}(1 + b_g^2\tan^2\theta) - 2k,$$

where Δ' measures the drive for tearing perturbations [27]. Using the standard matching approach [13,29] to the kinetic resonance layer gives

$$\frac{\gamma}{k v_{\mathrm{the}}} \approx \frac{d_e^2\Delta'}{2\sqrt{\pi}\, l_s[1 + \sqrt{m_eT_e/(m_iT_i)}]}, \qquad (1)$$

where $v_{\mathrm{the}} \equiv (2T_e/m_e)^{1/2}$ is the electron thermal speed, $d_e \equiv c/\omega_{pe}$ is the electron inertial length, $\omega_{pe} = (4\pi e^2 n_0/m_e)^{1/2}$ is the plasma frequency, and l_s is the scale length for variation in $k_\parallel = \mathbf{k}\cdot\mathbf{B}/|\mathbf{B}|$ given by

$$\frac{1}{l_s} \equiv \frac{1}{k}\left(\frac{dk_\parallel}{dz}\right)_{z=z_s} = \frac{\cos^2\theta - b_g^2\sin^2\theta}{\lambda\cos\theta(1 + b_g^2)^{1/2}}.$$

Since $\omega \propto \mathbf{k}\cdot\mathbf{U}_e \approx 0$ in the resonance layer, the real frequency vanishes and the modes are purely growing. Tearing perturbations are unstable for $\Delta' > 0$ corresponding to $k\lambda < k_c\lambda \approx (1 + b_g^2\tan^2\theta)^{1/2}$ and $|\theta| < \theta_c \approx \tan^{-1}(1/b_g)$. The shortest wavelength mode is $k\lambda \approx \sqrt{2}$ at $\theta = \theta_c$, while the most unstable modes are predicted to be oblique when $b_g > b_{g,c} = \sqrt{1/[2(k\lambda)^2] - 1/2}$. For modes with $k\lambda \approx 0.5$ this gives $b_{g,c} \approx 1.2$ corresponding to magnetic shear angles $\phi \lesssim 80°$. At this wavelength, the theory predicts oblique growth rates that are only $\sim$2% faster for $b_g = 4$, but the effect becomes stronger for shorter wavelengths.

To test this theory, fully kinetic simulations were performed using the VPIC code [30]. Unless otherwise stated, all simulations have parameters $v_{\mathrm{the}}/c = 0.21$ and $\omega_{pe}/\Omega_{ce} = 2$, where $\Omega_{ce} = eB_0/(m_ec)$, which implies $\beta_e \equiv 8\pi n_0T_e/B^2 = 0.18/(1 + b_g^2)$. Spatial scales are normalized by either d_e or $d_i = d_e(m_i/m_e)^{1/2}$ and time is normalized by $\Omega_{ci} = eB_0/(m_ic)$. Boundary conditions are periodic in the x and y directions, while the z boundaries are treated as a perfect reflecting conductor. A series of 2D simulations were performed with fixed $L_x = 4\pi\lambda$ corresponding to $k\lambda \approx 0.5$ to independently measure the tearing growth rate at each resonance surface. This was done by rotating the initial 1D equilibrium about the z axis by an angle θ in order to select a resonance surface. As illustrated in Fig. 1, a range of guide fields $b_g = 0 \to 4$, mass ratios $m_i/m_e = 1$–1836, and scale thicknesses were considered. For this range of parameters, the instability is always localized about the resonance surface and produces magnetic islands consistent with tearing. The measured growth rates in Fig. 1 are within a factor of $\sim$2 of Eq. (1) for the angular dependence. However, the decrease in the growth rate with increasing guide field is somewhat weaker in the simulations than predicted by Eq. (1). More importantly, the simulation growth rates at oblique angles are larger than Eq. (1) for stronger guide fields $b_g \gtrsim 1$. This trend is opposite that for the Harris equilibrium [13], where diamagnetic drifts may strongly influence the stability [13,31].

These 2D simulations demonstrate that tearing is the dominant instability, rather than the previously reported shear instability [15]. The only possible exception to the latter is for very low $\beta_e < 0.01$ regimes and narrow layers $\lambda \lesssim d_e$ (explored, but not shown), where the simulations feature a weaker growing instability with $k > k_c$

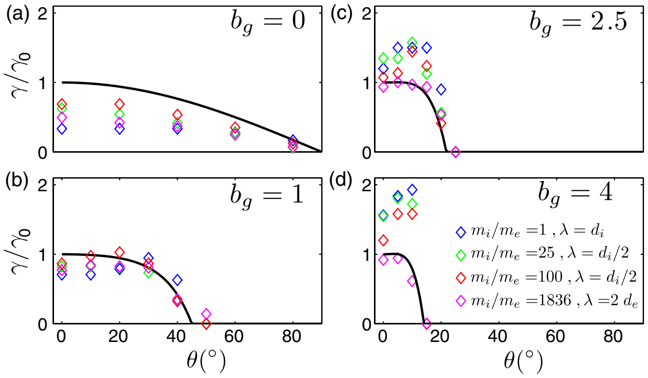

FIG. 1 (color online). Comparison of tearing mode growth rates from Eq. (1) (black line) with measured value from 2D kinetic simulations (diamonds) as a function of oblique angle θ with $k\lambda = 0.5$ fixed, and for the different guide fields, mass ratios, and initial layer thicknesses. All growth rates are normalized by γ_0, the theoretical value at $\theta = 0$.

corresponding to $\Delta' < 0$ where tearing should be stable. However, in contrast to the shear instability, this mode is localized about the resonance surfaces and produces magnetic islands, but is too weak to play any significant role for the parameters in this Letter.

While Eq. (1) roughly captures the magnitude and range of angles for the tearing instability, the oblique modes in the simulations grow even faster than predicted for guide fields $b_g > 1$. Since this physics persists into the nonlinear regime, it has immediate implications for the 3D structure of the diffusion region. To demonstrate this effect, we compare small 3D simulations ($L_x = L_z = 4\pi\lambda$) with $b_g = 2.5$ and the same initial conditions, and only change the system size L_y. The simulation in Fig. 2(a) with $L_y = 8\lambda$ only permits a single resonance layer at $z_s = 0$ and thus leads to a current density consistent with previous 2D models. In contrast, the simulation in Fig. 2(b) with $L_y = 46.9\lambda$ permits unstable modes at $z_s = 0, \pm 0.86\lambda$ corresponding to $\theta = 0°, \mp 15°$. Initialized with a weak seed, the two oblique modes dominate the evolution leading to enhanced current density at the respective resonance layers as shown in Fig. 2(b).

The persistence of this physics into the nonlinear regime is responsible for driving electron diffusion regions with multiple current sheets. However, the existence of other competing instabilities may complicate this picture. To examine this possibility, an additional 3D simulation was performed with the same parameters of Figs. 2(a) and 2(b), but with system size $L_x = 3.8L$ such that $\Delta' < 0$ for all modes. In this case, there was no evidence of any instability growth (not shown). Next, we performed a series of 3D simulations for electron-scale current sheets. The fluctuation spectrum is given in Fig. 2(c) for one example with $m_i/m_e = 1836$, $\lambda = 2d_e$, and $L_x = L_y = 24\pi\lambda$ to permit ~ 6 tearing modes with $k\lambda \approx 0.5$. The dominant fluctuations are well bounded by the marginal tearing criterion $\Delta' > 0$ (black lines). The only clear evidence of additional instabilities occurs when the streaming exceeds the Buneman threshold [23,24] of $U_{ey} > \sqrt{2}v_{\mathrm{the}}$ (for $T_i = T_e$), which requires very thin layers $\lambda < d_e/[2\beta_e(1 + b_g^2)]^{1/2}$. While the example in Fig. 2(c) is slightly below this threshold, reducing the layer thickness to $\lambda = d_e$ results in a strong Buneman instability that broadens the layer (not shown), but over longer times the tearing modes still dominate.

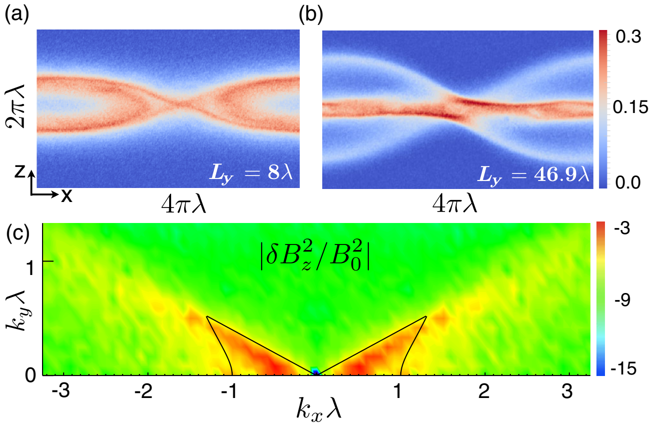

FIG. 2 (color online). Comparison of current density $\mathbf{J}$ at $t\Omega_{ci} = 16$ from two 3D simulations with initial conditions $b_g = 2.5$, $m_i/m_e = 25$, $\lambda = 0.5d_i$, $\beta_e = 0.025$, and with (a) $L_y = 8\lambda$ to allow a single resonance surface at $z_s = 0$ and (b) $L_y = 46.9\lambda$ to allow three resonance surfaces $z_s = 0, \pm 0.86\lambda$. (c) Spectrum of $|\delta B_z^2/B_0^2|$ from a simulation with $\lambda = 2d_e$, $m_i/m_e = 1836$, $b_g = 2.5$, and system size $24\pi\lambda \times 24\pi\lambda \times 3\pi\lambda$. The observed fluctuations are predominantly for wave vectors with $\Delta' > 0$ where tearing is unstable (black).

To understand how these results apply to larger 3D systems, we performed four simulations with varying guide field $b_g = 0.5$, 1, 2.5, 4 for $m_i/m_e = 100$, $\lambda = 0.5d_i$, and system size $40d_i \times 40d_i \times 15d_i$ corresponding to $2048 \times 2048 \times 1024$ cells and $\sim 10^{12}$ particles. Consistent with the results in Fig. 1, the cases with $b_g < b_{g,c} \approx 1.2$ did not produce multiple electron layers in the diffusion region. Because of limited space, here we focus on the cases with $b_g > b_{g,c}$. The $b_g = 2.5$ simulation is dominated by oblique flux ropes as shown in Fig. 3(a) leading to diffusion regions with multiple electron current layers as illustrated in Fig. 3(b). Notice that the electron current sheets are oriented at angles $\theta \approx \pm 11°$ roughly consistent with the fastest growing oblique tearing modes [see Fig. 1(c)], suggesting that the 3D morphology is determined by similar physics. This is surprising since the profiles have changed dramatically from the initial condition. However, the total magnetic shear across the layer is fixed and the fastest growing modes in Fig. 1 occur at roughly the same oblique angles in both ion and electron-scale layers, which may explain the persistence of this angle.

The diffusion region illustrated in Fig. 3(b) consists of two electron layers embedded within a single ion layer which seems to be the most common configuration for $b_g \gtrsim b_{g,c}$ regimes. However, it is possible to find examples with a single electron layer, and still others with three or more electron layers. Two additional examples are illustrated in Fig. 4 for the strongest guide field simulation $b_g = 4$ ($\beta_e \approx 0.01$) at the two times indicated. This simulation has the same domain size as in Fig. 3 but with a finer spatial grid ($2048 \times 2048 \times 1536$) and $\sim 1.5 \times 10^{12}$ particles. The current density in Fig. 4(a) features two electron layers each with transverse scale $\approx 0.45d_e$ (measured by half-width at half-maximum) while the example shown in Fig. 4(b) consists of three layers with similar thickness. In both cases, the ion streamlines (white) shows a clear inflow and outflow associated with reconnection. Measured in terms of the local electron gyroradius, the half-thickness of these layers is (2.5–3.5)ρ_e, which is comparable to the layers near the x-line in 2D. The peak agyrotropy [26] is 0.12, which is slightly larger than the corresponding 2D simulation.

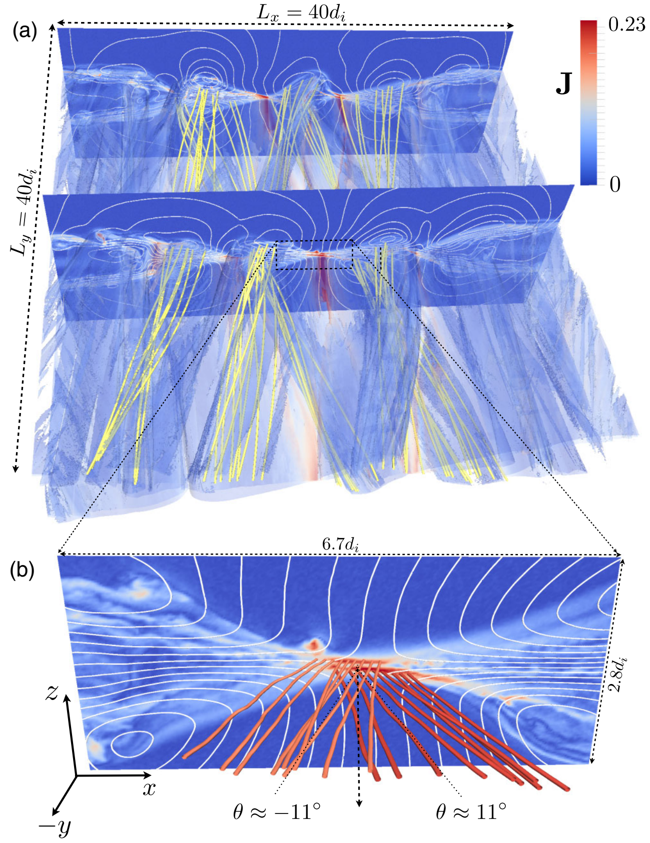

FIG. 3 (color online). (a) Three-dimensional structure of reconnection for the large simulation with $m_i/m_e = 100$, $b_g = 2.5$, $\beta_e = 0.025$ at $t\Omega_{ci} = 36$. Shown is an isosurface of particle density, colored by the current density along with sample magnetic field lines (yellow). Cutting planes also show the current along with streamlines of the in-plane ion flow velocity (white). (b) Closeup of the electron diffusion region along with sample streamlines of the current density (red).

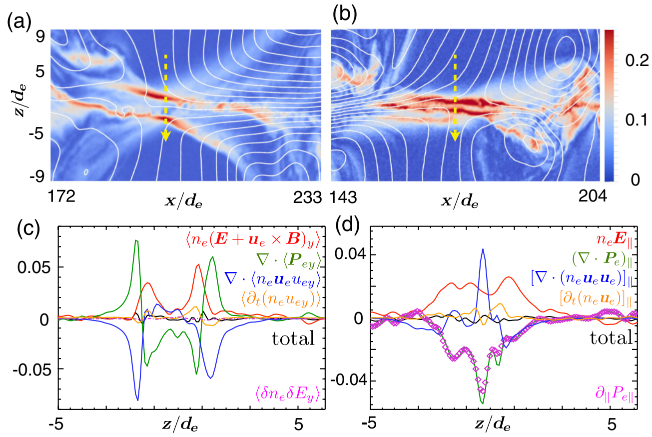

FIG. 4 (color online). (a) Current density **J** within the diffusion region and ion streamlines (white) for the large 3D simulation with $m_i/m_e = 100$, $b_g = 4$, and $\beta_e \approx 0.01$ at $t\Omega_{ci} = 44$. (b) Example of a diffusion region with three electron layers from the same simulation at later time $t\Omega_{ci} = 65$. (c) Terms in the time-averaged electron momentum equation evaluated along the line indicated in (a) along with the anomalous resistivity $\langle \delta n_e \delta E_y \rangle$. (d) Dominant terms balancing the parallel electric field $E_\parallel$ along the line indicated in (b). In both (c) and (d) all terms are normalized by $n_0 V_A B_0 / c$ where $V_A = B/\sqrt{4\pi m_i n_0}$.

To examine the dissipation physics, each term in the electron momentum equation was evaluated and time averaged over an interval $1/\Omega_{ci}$ (corresponding to 625 time slices). The y component of each term is shown in Fig. 4(c) across the layer as indicated. The peak nonideal electric field (red) inside the layers is balanced predominantly by the divergence of the pressure tensor $\nabla \cdot \mathbf{P}_e$ (green). For the example shown, there is a strong cancellation between $\nabla \cdot \mathbf{P}_e$ and the inertial term (blue), but for other slices there are regions in which the inertial terms dominate. Separating quantities into a mean and fluctuating component, the anomalous resistivity (purple) arising from $\langle \delta n_e \delta E_y \rangle$ is typically quite small $\lesssim 5\%$.

The results in Fig. 4(d) were computed in the same manner, but for the parallel component of the momentum balance across the three electron layers as indicated in Fig. 4(b). The parallel electric field $E_\parallel$ is supported by the combined influence of electron inertia and the pressure tensor. To understand this further, it is useful to decompose the pressure tensor into a portion that is cylindrically symmetric (i.e., gyrotropic) about the local magnetic field $\mathbf{P}_{eg} \equiv P_{e\perp}\mathbf{I} + (P_{e\parallel} - P_{e\perp})\mathbf{bb}$ so that we can write $(\nabla \cdot \mathbf{P}_{eg})_\parallel = \partial_\parallel P_{e\parallel} - (P_{e\parallel} - P_{e\perp})\partial_\parallel \ln|B|$, where $\partial_\parallel \equiv \mathbf{b} \cdot \nabla$ and $\mathbf{b} \equiv \mathbf{B}/|B|$. Evaluating these contributions from $P_{e\parallel} \equiv \mathbf{b} \cdot \mathbf{P}_e \cdot \mathbf{b}$ and $P_{e\perp} \equiv [\mathrm{Tr}(\mathbf{P}_e) - P_{e\parallel}]/2$ demonstrates that in most regions $(\nabla \cdot \mathbf{P}_e)_\parallel \approx \partial_\parallel P_{e\parallel}$ with significant differences occurring only inside the electron layers where the pressure tensor is nongyrotropic, similar to recent spacecraft observations [32]. While intense streaming is clearly evident, reconnection drives strong parallel heating in low-β regimes [25], resulting in layers that are marginally below the Buneman threshold. There is no evidence that shear instabilities broaden these layers or alter the dissipation physics. Instead, it appears the electron pressure tensor provides ample flexibility for breaking the frozen-flux constraint in low $\beta_e \gtrsim 0.01$ regimes.

Despite the rich 3D dynamics, the energy conversion time scale is nearly the same as 2D. To quantify the 3D reconnection rate, one leading idea [33] involves computing $\langle E_\parallel \rangle = \int E_\parallel ds$ along field lines passing through the diffusion region back into an ideal region where $E_\parallel = 0$. Applying this approach is complicated by the fact that the magnetic field lines are chaotic and it is difficult to identify a transition back into an ideal region. Instead, we selected 20 seed points along the central electron sheet in Fig. 4(b) and integrated $E_\parallel$ along these magnetic field lines once through the system. The resulting average $\langle E_\parallel \rangle \approx 0.023 V_A B_0/c$ is very close to the corresponding 2D simulation near the x-line $E_\parallel \approx 0.025 V_A B_0/c$, indicating the rates are nearly the same. However, this does not imply that all details of the energy conversion are the same. In particular, the 3D dynamics drives turbulence characterized by a power law with a break at the electron scale and there is preliminary evidence that more electrons are accelerated into the energetic tails. Details of these results will be reported in future publications.

We are grateful for support from NASA through the Heliophysics Theory program, DOE/OFES through CMSO, and from the LDRD program at LANL. Contributions from H. K. and V. R. were supported by NASA Grant No. NNH11CC65C, and NSF through EAGER 1105084. This research is part of the Blue Waters sustained-petascale computing project, which is supported by the NSF (OCI 07-25070) and the state of Illinois. Additional simulations were performed at the National Center for Computational Sciences at ORNL and with LANL institutional computing. We thank Burlen Loring for visualization assistance with ParaView.

[1] H. Ji and W. Daughton, Phys. Plasmas **18**, 111207 (2011).
[2] J. Birn, J. F. Drake, M. A. Shay, B. N. Rogers, R. E. Denton, M. Hesse, M. Kuznetsova, Z. W. Ma, A. Bhattacharjee, A. Otto, A. Otto, and P. L. Pritchett, J. Geophys. Res. **106**, 3715 (2001).
[3] D. Biskamp, *Magnetic Reconnection in Plasmas* (Cambridge University Press, Cambridge, England, 2000).
[4] M. Hesse, K. Schindler, J. Birn, and M. Kuznetsova, Phys. Plasmas **6**, 1781 (1999).
[5] P. Pritchett, J. Geophys. Res. **106**, 3783 (2001).
[6] P. Ricci, J. U. Brackbill, W. Daughton, and G. Lapenta, Phys. Plasmas **11**, 4102 (2004).
[7] W. Daughton, J. Scudder, and H. Karimabadi, Phys. Plasmas **13**, 072101 (2006).
[8] H. Karimabadi, W. Daughton, and J. Scudder, Geophys. Res. Lett. **34**, L13104 (2007).
[9] M. A. Shay, J. F. Drake, and M. Swisdak, Phys. Rev. Lett. **99**, 155002 (2007).
[10] A. Klimas, M. Hesse, and S. Zenitani, Phys. Plasmas **15**, 082102 (2008).
[11] A. A. Galeev, M. M. Kuznetsova, and L. M. Zelenyi, Space Sci. Rev. **44**, 1 (1986).
[12] K. Bowers and H. Li, Phys. Rev. Lett. **98**, 035002 (2007).
[13] W. Daughton, V. Roytershteyn, H. Karimabadi, L. Yin, B. J. Albright, B. Bergen, and K. J. Bowers, Nat. Phys. **7**, 539 (2011).
[14] V. Roytershteyn, W. Daughton, H. Karimabadi, and F. S. Mozer, Phys. Rev. Lett. **108**, 185001 (2012).
[15] H. Che, J. F. Drake, and M. Swisdak, Nature (London) **474**, 184 (2011).
[16] E. N. Parker, Astrophys. J. **264**, 642 (1983).
[17] D. A. Falconer, R. L. Moore, J. G. Porter, G. A. Gary, and T. Shimizu, Astrophys. J. **482**, 519 (1997).
[18] T. D. Phan, J. T. Gosling, G. Paschmann, C. Pasma, J. F. Drake, M. Øieroset, D. Larson, R. P. Lin, and M. S. Davis, Astrophys. J. **719**, L199 (2010).
[19] J. T. Gosling, R. P. Lin, and A. Szabo, Geophys. Res. Lett. **34**, L15110 (2007).
[20] T. D. Phan, G. Paschmann, C. Twitty, F. S. Mozer, J. T. Gosling, J. P. Eastwood, M. Øieroset, H. Rème, and E. A. Lucek, Geophys. Res. Lett. **34**, L14104 (2007).
[21] J. T. Gosling, M. F. Thomsen, S. J. Bame, R. C. Elphic, and C. T. Russell, J. Geophys. Res. **96**, 14097 (1991).
[22] J. Slavin *et al.*, J. Geophys. Res. **117**, A00M06 (2012).
[23] O. Buneman, Phys. Rev. **115**, 503 (1959).
[24] B. Fried and R. Gould, Phys. Fluids **4**, 139 (1961).
[25] J. Egedal, A. Le, and W. Daughton, Phys. Plasmas (to be published).
[26] J. D. Scudder and W. Daughton, J. Geophys. Res. **113**, A06222 (2008).
[27] H. Furth, J. Killeen, and M. N. Rosenbluth, Phys. Fluids **6**, 459 (1963).
[28] S. D. Baalrud, A. Bhattacharjee, and Y. M. Huang, Phys. Plasmas **19**, 022101 (2012).
[29] J. F. Drake and Y. C. Lee, Phys. Fluids **20**, 1341 (1977).
[30] K. Bowers, B. Albright, L. Yin, W. Daughton, V. Roytershteyn, B. Bergen, and T. Kwan, J. Phys. Conf. Ser. **180**, 012055 (2009).
[31] S. D. Baalrud, A. Bhattacharjee, and W. Daughton, Phys. Plasmas (to be published).
[32] J. D. Scudder, R. D. Holdaway, W. Daughton, H. Karimabadi, V. Roytershteyn, C. T. Russell, and J. Y. Lopez, Phys. Rev. Lett. **108**, 225005 (2012).
[33] M. Hesse, T. Forbes, and J. Birn, Astrophys. J. **631**, 1227 (2005).